TCAD analysis of GaN HEMT AC parameters through accurate solution of trap rate equations

TCAD analysis of GaN HEMT AC parameters through accurate solution of trap rate equations

E. Catoggio[#1], S. Donati Guerrieri[#2], F. Bonani[#3]

[#]Dipartimento di Elettronica e Telecomunicazioni, Politecnico di Torino, Italy

[1]eva.catoggio, [2]simona.donati, [3]fabrizio.bonani@polito.it

Abstract—Physics-based simulations allow for an accurate insight into the impact of trap dynamics on GaN HEMT performance. In particular, traps are responsible for the low-frequency dispersion of AC performance, e.g. the Y parameters. In this paper we present an in-house TCAD simulator implementing the trap rate equations coupled to the drift-diffusion physical model and solved through the Harmonic Balance algorithm. The developed TCAD allows for the extraction of the trap rate equations Green's Functions (GFs) in the frequency domain. GFs are then used to compute the sensitivity of the AC Y parameters towards variations of the trap physical parameters (e.g. the trap energy) and to extract the *local sensitivity* showing the parts of the device where traps influence most the HEMT AC parameters.

Keywords—GaN HEMTs, Nonlinear device models, TCAD simulations, Trap rate equations, Scattering Parameters

I. Introduction

GaN HEMT technology is rapidly achieving sufficient maturity for its exploitation in communication and space power applications, although trap dynamics still is a bottleneck limiting RF/microwave power performance [1]. Various characterization techniques aim at identifying the trap dynamic behaviour, linking the trap occupation to the gate/drain current delay in terms e.g. of rise/fall time in the response to specific stimuli such as voltage steps or pulses [2], [3]. Pulsed S parameters are also used to assess the trap-related dispersion of AC and RF parameters [4], [5]. In fact, the peculiar low frequency dispersion of the device Y parameters has become a standard method to characterize the trap dynamics [6]. While characterizations typically provide only the dynamics of the device terminal currents, TCAD analysis represents a unique opportunity to investigate the effect of the trap localization, especially when trap density varies in the device volume. In this work, we present an in-house TCAD simulator implementing explicitly the trap rate equations coupled to the drift-diffusion (DD) physical model and solved through the Harmonic Balance (HB) algorithm. In this implementation, no back-substitution of the trap equations is performed, so as to maintain a fully general model. The developed TCAD allows for both the LS and SS-LS device physical analysis along with the extraction the Green's Functions (GFs) of the physical model in the frequency domain. In particular, we exploit the GFs of the trap rate equations, not currently available in commercial codes. We demonstrate that these GFs are a powerful tool to: 1) compute the sensitivity of the AC parameters towards variations of the trap physical parameters (e.g. the trap concentration and trap energy) in a numerically efficient way; 2) extract the *local sensitivity* showing the areas of the device where traps influence most the HEMT AC features. We apply the implemented model to a Fe-doped GaN HEMT, investigating the dependency of Y-parameters on the trap energy.

II. Trap dynamic model implementation

For each trap, the Trap Rate Equation (TRE) reads [7]:

$$\frac{\partial f^n}{\partial t} = (1 - f^n)c_C^n - f^n e_C^n + (1 - f^n)e_V^p - f^n c_V^p \qquad (1)$$

where f^n is the electron occupation probability, c_C^n and e_C^n the electron capture and emission rates to the conduction band and c_V^p and e_V^p the hole capture and emission rates to the valence band. According to the principle of detailed balance:

$$c_C^n = {}_n v_{th}^n n; \quad e_C^n = {}_n v_{th}^n n_1$$
$$c_V^p = {}_p v_{th}^p p; \quad e_V^p = {}_p v_{th}^p p_1$$

where ${}_n$ and ${}_p$ denote the trap cross sections, v_{th}^n and v_{th}^p the thermal velocities, $n_1 = N_C \exp[(E_T - E_C)/k_B T]$ and $p_1 = N_V \exp[(E_V - E_T)/k_B T]$, being E_T the trap energy level. Here we present the modelling approach with one trap only, but the generalization to the case of several traps is obvious. In the in-house developed TCAD, f^n is expressed as the ratio between the concentration of occupied traps n_T and the local trap concentration N_T, hence TRE becomes:

$$\frac{\partial n_T}{\partial t} = \underbrace{N_T\left(1 - \frac{n_T}{N_T}\right)c_C^n}_{R_n} - \underbrace{N_T\frac{n_T}{N_T}e_C^n}_{G_n} + \underbrace{N_T\frac{n_T}{N_T}c_V^p}_{R_p} - \underbrace{N_T\left(1 - \frac{n_T}{N_T}\right)e_V^p}_{G_p} = \underbrace{R_n - G_n}_{U_n} - \underbrace{(R_p - G_p)}_{U_p} = U_n - U_p \qquad (2)$$

where U_n and U_p denote the net recombination rates. TRE couples to the DD model due to the trap charge qn_T in Poisson equation:

$$\nabla \cdot (\varepsilon \nabla) = q\,(p - n + N_D - N_A - n_T) \qquad (3)$$

and due to the trap recombination rates in the carrier continuity equations:

$$\frac{1}{q}\nabla \cdot J_n = \frac{\partial n}{\partial t} + U_n \qquad \frac{1}{q}\nabla \cdot J_p = \frac{\partial p}{\partial t} + U_p \qquad (4)$$

Finally, the coupled DD-TRE system (3), (4) and (2) allows to self-consistently model the effect of trap dynamics on the device electrical features.

In steady-state conditions ($\partial n_{\mathsf{T}}/\partial t = 0$) TRE uncouples from the DD system leading to the classical Shockley-Read-Hall model, while in the dynamic case DD-TRE must be solved self-consistently. Time-domain approaches aim at mimicking the measurements with pulses and voltage steps, but frequency domain analyses are more adherent to the final device operating conditions. In this work the DD-TRE model, treated in the frequency-domain through the HB approach, can be cast into the form

$$\mathbf{D}^{(\alpha)}\dot{\mathbf{x}} = \mathbf{F}^{(\alpha)}(\mathbf{x}, \mathbf{e}; \boldsymbol{\sigma}) \qquad \alpha = \varphi, n, p, n_{\mathsf{T}} \tag{5}$$

where $\alpha = \varphi$ refers to the Poisson equation (3), $\alpha = n, p$ to the electron and hole continuity equations (4), and $\alpha = n_{\mathsf{T}}$ to the trap rate equation (2). Vector $\mathbf{x}$ collects the nodal values of the discretized potential φ, carrier densities n and p and trap charge n_{T} while $\dot{\mathbf{x}}$ denotes the corresponding time derivatives. $\mathbf{D}^{(\alpha)}$ is a diagonal matrix accounting for the time-derivatives of the system (memory) while $\mathbf{F}$ is the memory-less part [9]. In the HB analysis, the external sources $\mathbf{e}$ correspond to the superposition of DC + harmonic stimuli with fundamental frequency f_0, thereby forcing the device in periodic large-signal operation. In (5) vector $\boldsymbol{\sigma}$ represents the collection of the model parameters such as e.g. trap energy, cross section, total concentration.

Following the HB approach, $\mathbf{x}(t)$ is Fourier expanded as[1]:

$$\mathbf{x}(t) = \sum_{\mathsf{k}=-\mathsf{N_H}}^{\mathsf{N_H}} \mathbf{X}_{\mathsf{k}} \exp(\mathrm{j}k\omega_0 t) \tag{6}$$

where $\omega_0 = 2\pi f_0$, $\mathbf{X}_{\mathsf{k}}$ is the phasor of the k-th harmonic ($X_{-\mathsf{k}} = X_{\mathsf{k}}^*$ for each k, where * denotes complex conjugation), while (5) is converted into the frequency domain as:

$$\mathbf{D}^{(\alpha)}\boldsymbol{\Omega}\mathbf{X} = \boldsymbol{\Gamma}\mathbf{F}^{(\alpha)}(\boldsymbol{\Gamma}^{-1}\mathbf{X}, \mathbf{E}; \boldsymbol{\sigma}) \qquad \alpha = \varphi, n, p, n_{\mathsf{T}} \tag{7}$$

where $\mathbf{E}$ is the collection of the harmonic amplitudes of the applied generators $\mathbf{e}(t)$, $\boldsymbol{\Omega}$ is an operator representing time derivation in the frequency domain, and $\boldsymbol{\Gamma}^{-1}$ is the operator implementing the dicrete Fourier tranform (6) between phasors and time samples. The solution $\mathbf{X}_{\mathrm{S}}$ of (7) with nominal parameters $\boldsymbol{\sigma}_0$ includes all the harmonic amplitudes of the large-signal steady-state of the nominal device.

In this contribution, we consider a particular case for (7) that corresponds to AC analysis, where the input generators $\mathbf{E}$ contain only a DC component and a single tone at frequency f_0. The tone amplitude is small enough to assume a linear response of the device, therefore the full system (7) is solved *without* any linearization, but the expansion (6) is limited to $N_{\mathrm{H}} = 1$. The tone is recursively applied to each device terminal r yielding a corresponding current $i^{(\mathsf{q})}$ at each terminal q. The DC component $I_0^{(\mathsf{q})}$ corresponds to the DC working point of the AC analysis, while the phasor $I_1^{(\mathsf{q})}$ at fundamental frequency allows to compute the (q, r) element of the AC admittance matrix as

$$Y_{\mathsf{q};\mathsf{r}} = \frac{I_1^{(\mathsf{q})}}{V_1^{(\mathsf{r})}} \tag{8}$$

Assuming a (time-independent) perturbation $\Delta\boldsymbol{\sigma} = \boldsymbol{\sigma} - \boldsymbol{\sigma}_0$ of the model parameters, a *linearization* of (7) allows for the sensitivity analysis of AC parameters [8]. Denoting with $\Delta I_1^{(\mathsf{q})}$ the variation of the current phasor at terminal q induced by $\Delta\boldsymbol{\sigma}$, the Green's Function approach allows to write

$$\Delta I_1^{(\mathsf{q})} = \sum_{\alpha} \int_{\Omega} \left(\mathbf{G}_{\alpha}^{(\mathsf{q})}(\mathbf{r})\right)_{(1;1)} \mathbf{S}_{\alpha;1}(\mathbf{r})\ \mathrm{d}\mathbf{r} \tag{9}$$

where $(\mathbf{G}_{\alpha}^{(\mathsf{q})}(\mathbf{r}))_{(1;1)}$ is the (1,1) element of the Conversion Green's Function (CGF) [9], while $\mathbf{S}_{\alpha;1}(\mathbf{r})$ represents a microscopic (local) source at fundamental frequency, computed as the residual of (7) for a variation $\Delta\boldsymbol{\sigma}$ (see [8] for details). The integrand function of the spatial convolution (9) represents the *local variation source* $K_{\alpha}^{(\mathsf{q})}(\mathbf{r}) = \left(\mathbf{G}_{\alpha}^{(\mathsf{q})}(\mathbf{r})\right)_{(1;1)} \mathbf{S}_{\alpha;1}(\mathbf{r})$, i.e. a map of the device internal regions allowing to identify where physical parameter variations influence most the device characteristics. According to (8) and (9), $K_{\alpha}^{(\mathsf{q})}(\mathbf{r})/V_1^{(\mathsf{r})}$ corresponds to the distributed variation source, whose integral yields $\Delta Y_{\mathsf{q};\mathsf{r}} = \Delta I_1^{(\mathsf{q})}/V_1^{(\mathsf{r})}$, i.e. the variation of the (q, r) element of the Y matrix discussed in detail in section III.

III. Results

We consider the 0.150 μm gate length HEMT structure in Fig. 1, including the AlGaN barrier layer (15 nm thickness, Al mole fraction 25%) and the GaN layer, which has been divided into a 5 nm thick channel region (with residual donor doping of 10^{15} cm^{-3}) and a 2 μm deep buffer region, characterized by a Fe doping with concentration $N_{\mathrm{T}} = 10^{18}$ cm^{-3}. Fig. 1 shows the details of the HEMT structure, including the source and drain doped regions and the S/D contacts. The simulation includes the GaN spontaneous polarization and both the AlGaN spontaneous and piezoelectric polarization. The resulting net polarization charge at the AlGaN/GaN interface is $\sigma_{\mathrm{pol}} = 1.34 \times 10^{13}$ cm^{-2}, with 90% activation. For further details on the polarization model the reader can refer to the Synopsys `Simplified strain model` [10], which was implemented in our in-house simulator. The polarization charge at the interface with the contacts and the passivation layers has been exactly compensated. A fixed interface negative charge $\sigma_{\mathrm{int}} = -2 \times 10^{12}$ cm^{-2} has been also added to the barrier/passivation interface. The electron mobility includes dependency on lattice temperature and doping, while velocity saturation is modelled with the Caughey-Thomas model with $v_{\mathsf{n;sat}} = 2.5 \times 10^7$ cm/s for both AlGaN and GaN. The simulated device is characterized by the threshold voltage $V_{\mathsf{th}} = -2.5$ V and $I_{\mathsf{Dss}} = 1.2$ A/mm saturation current.

Fe doping acts like a deep acceptor-like trap with trap energy $E_{\mathrm{T}} = E_{\mathrm{C}} - 0.45\,\mathrm{eV}$ (being E_{C} the conduction band edge) and electron and hole capture cross-sections $\sigma_{\mathsf{n}} = \sigma_{\mathsf{p}} =$

[1]We consider here a purely periodic signal for the sake of simplicity. The extension to the quasi-periodic case is trivial.

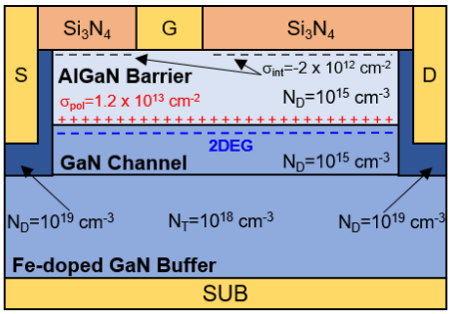

Thickness		Length	
Si_3N_4	100 nm	Gate	150 nm
AlGaN barrier	15 nm	Gate-Source	800 nm
GaN channel	5 nm	Gate-Drain	2000 nm
Gate buffer	2000 nm		

Fig. 1: Simulated HEMT structure.

3×10^{-16} cm^2. We aim at investigating the effect of Fe trap dynamics on the HEMT Y parameters. The DC bias point is set to $V_{\mathrm{D}} = 10$ V and $V_{\mathrm{G}} = -2.22$ V, corresponding to $10\% I_{\mathrm{D\,ss}}$. i.e. similar to the typical bias condition for power amplifiers.

The Y-parameters were extracted from the in-house code as described in Sec. II with $N_{\mathrm{H}} = 1$ and an input tone of 1 mV amplitude recursively applied to each terminal. The tone frequency was swept from 10 Hz to 1 MHz. At each frequency, the Y matrix and the CGFs are calculated with nominal Fe trap energy $E_{\mathrm{trap}} = 0.45$ eV from conduction band. The variations of the Y parameters are then evaluated according to (9) with varied values $E_{\mathrm{trap}} = [0.445, 0.455]$ eV. For validation, results of the GF approach are also compared to repeated AC simulations with varying trap energy levels (incremental method, INC, more numerically intensive), always obtaining an excellent agreement. Fig. 2 shows that Fe-doped traps are responsible of a positive peak at $f_{\mathrm{peak}} \approx 2$ kHz in the imaginary part of Y_{22}. With decreasing E_{trap}, the peak is shifted towards higher frequency values and $\mathrm{Imag}\{Y_{22}\}$ slightly increases. To achieve a further insight on these results, we investigate which parts of the device contribute to the Y_{22} variations. The dominant contribution stems from the local variation sources of the trap rate equation $K_{\mathsf{n}_T}^{(\mathsf{D})}$, hence we report the imaginary part of $K_{\mathsf{n}_T}^{(\mathsf{D})}/V_1^{(\mathsf{D})}$, whose integral yields $\mathrm{Imag}\{\Delta Y_{22}\}$. Figures 3 and 4 show the distributed variation source for $E_{\mathrm{trap}} = 0.455$ eV (5 meV variation with respect to the nominal value) for the two frequencies $f_1 < f_{\mathrm{peak}}$ and $f_2 > f_{\mathrm{peak}}$ shown in Fig. 2. In general the source is significant only in the buffer region below the gate. For the lower frequency the source is more concentrated at the source side of the channel and assumes positive values. At higher frequency, the local variation extends towards the drain contact and becomes negative.

Fig. 5 shows two frequency peaks in the imaginary part of Y_{21} [6]: a positive peak at $f_{\mathrm{peak;a}} \simeq 250$ Hz and a negative peak $f_{\mathrm{peak,b}}$ at around 3 kHz due to buffer traps. With decreasing trap

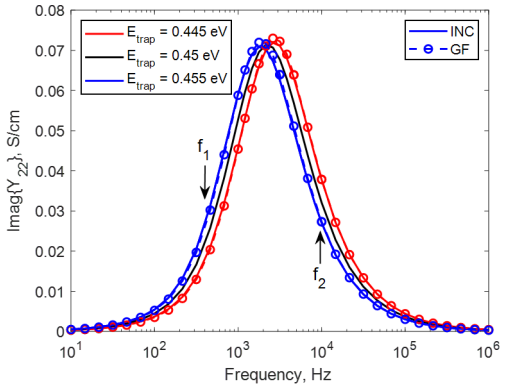

Fig. 2: Imaginary part of Y_{22} at different trap levels. Lines: INC approach. Symbols: GF approach.

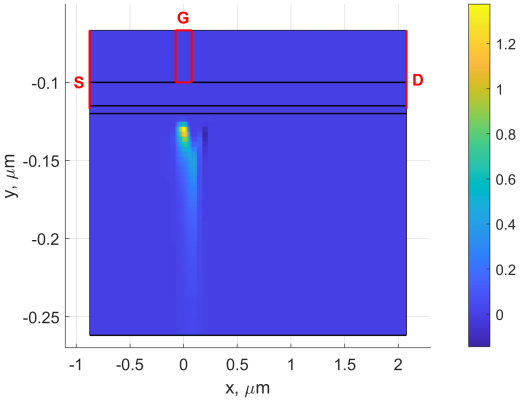

Fig. 3: Imaginary part of the local variation source of $\mathrm{Imag}\{\Delta Y_{22}\}$ [S/μm^2] at $f_1 = 464$ Hz reported in Fig. 2.

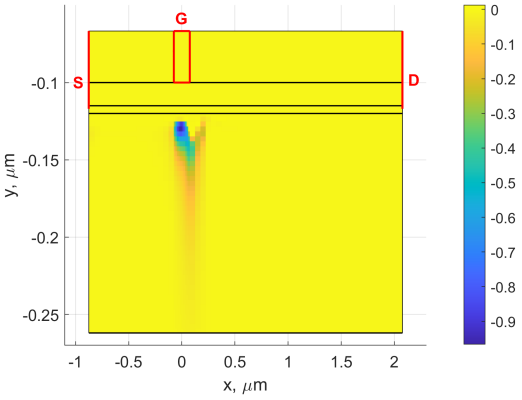

Fig. 4: Imaginary part of the local variation source of $\mathrm{Imag}\{\Delta Y_{22}\}$ [S/μm^2] at $f_2 = 10$ kHz reported in Fig. 2.

energy level, the buffer peak shifts towards higher frequencies while the positive one is almost insensitive to E_{trap} variations. Figures 6, 7 and 8 show the imaginary part of $K_{\mathsf{n}_T}^{(\mathsf{D})}/V_1^{(\mathsf{G})}$, i.e. the integrand function of $\mathrm{Imag}\{Y_{21}\}$, at three different frequencies. Increasing frequency from f_1 to f_3, the local variation source spreading becomes more widely distributed towards both the drain and the depth of the buffer region:

Fig. 5: Imaginary part of Y_{21} at different trap levels. Lines: INC approach. Symbols: GF approach.

in particular it has positive values at frequency $f_1 < f_{\text{peak,a}}$, mostly negative at f_2 while at $f_3 > f_{\text{peak,b}}$ we notice a sharp negative peak under the gate at source side and a broad positive region under the whole gate area.

IV. Conclusion

We presented an in-house TCAD simulator implementing the trap rate equations coupled to the DD model, allowing for the calculation of the trap rate equations Green's Functions in the frequency domain. The new code has been applied to the analysis of the Y-parameter low-frequency dispersion, showing the Y-parameter sensitivity to the trap energy and the corresponding local sensitivity.

The novel code opens the way to the GaN HEMT variability analysis (by randomization of individual traps position, energy and cross section) without the need of computationally intensive MonteCarlo analysis. Furthermore, the developed TCAD code is based on the direct solution of the trap equations coupled to the DD model through the HB algorithm. Therefore, the presented AC analysis can be readily extended to the dynamic large-signal analysis with no further code variations.

Acknowledgment

This work has been supported by the Italian Ministero dell'Istruzione, dell'Università e della Ricerca (MIUR) under the PRIN 2017 Project "Empowering GaN-on-SiC and GaN-on-Si technologies for the next challenging millimeter-wave applications (GANAPP)".

References

[1] G. Meneghesso et al., *IEEE Transactions on Device and Materials Reliability*, vol. 8, no. 2, pp. 332–343, Jun. 2008.
[2] N. Zagni et al., *Micromachines*, vol. 13, no. 12, p. 2244, Dec 2022.
[3] A. M. Angelotti et al., *IEEE Transactions on Electron Devices*, vol. 67, no. 8, pp. 3069–3074, Aug. 2020.
[4] P. Beleniotis et al., in *2022 17th European Microwave Integrated Circuits Conference (EuMIC)*. IEEE, Sep. 2022.
[5] J. L. Gomes et al., in *2020 International Workshop on Integrated Nonlinear Microwave and Millimetre-Wave Circuits (INMMiC)*. IEEE, Jul. 2020.
[6] P. V. Raja et al., *Electronics*, vol. 10, no. 24, p. 3096, Dec. 2021.

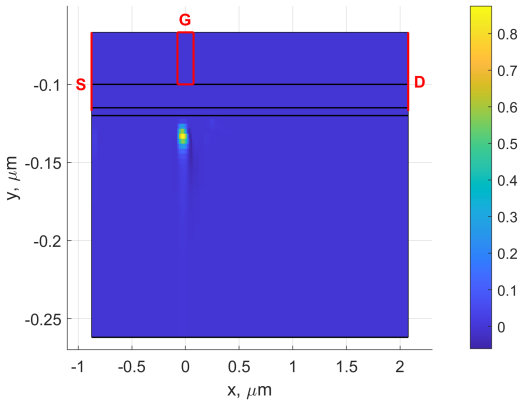

Fig. 6: Imaginary part of the local variation source of $\text{Imag}\{\Delta Y_{21}\}$ [S/μm^2] at $f_1 = 46$ Hz reported in Fig. 5.

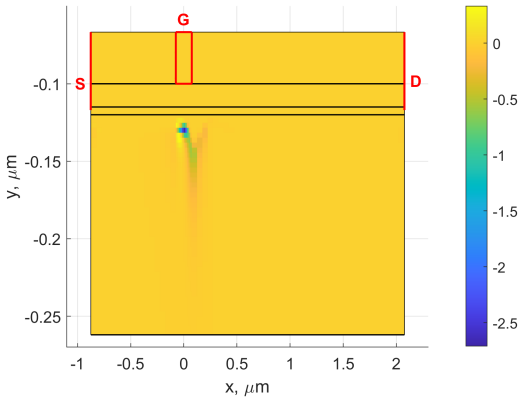

Fig. 7: Imaginary part of the local variation source of $\text{Imag}\{\Delta Y_{21}\}$ [S/μm^2] at $f_2 = 1$ kHz reported in Fig. 5.

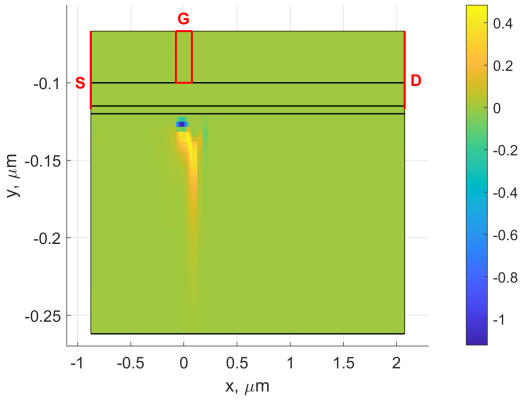

Fig. 8: Imaginary part of the local variation source of $\text{Imag}\{\Delta Y_{21}\}$ [S/μm^2] at $f_3 = 10$ kHz reported in Fig. 5.

[7] F. Bonani etal., *Solid-State Electronics*, vol. 43, no. 2, p. 285, Feb. 1999.
[8] F. Bonani et al., *IEEE Transactions on Electron Devices*, vol. 51, no. 3, pp. 477–485, Mar. 2004.
[9] F. Bonani et al. *IEEE Transactions on Electron Devices*, vol. 48, no. 5, pp. 966–977, May 2001.
[10] [Online]. Available: https://www.synopsys.com/silicon/tcad/device-simulation/sentaurus-device.html